Article

Surface-specific flow factors for prediction of friction of crosshatched surfaces

Leighton, M, Rahmani, R and Rahnejat, Homer

Leighton, M, Rahmani, R and Rahnejat, Homer ORCID: 0000-0003-2257-7102 (2016) Surface-specific flow factors for prediction of friction of crosshatched surfaces. Surface Topography: Metrology and Properties, 4 (1).

PAPER • **OPEN ACCESS**

Surface-specific flow factors for prediction of friction of cross-hatched surfaces

To cite this article: M Leighton *et al* 2016 *Surf. Topogr.: Metrol. Prop.* **4** 025002

Surface Topography: Metrology and Properties

OPEN ACCESS

RECEIVED
5 November 2015

REVISED
5 February 2016

ACCEPTED FOR PUBLICATION
5 February 2016

PUBLISHED
22 March 2016

PAPER

Surface-specific flow factors for prediction of friction of cross-hatched surfaces

M Leighton, R Rahmani and H Rahnejat

Wolfson School of Mechanical and Manufacturing Engineering, Loughborough University, Loughborough, UK

E-mail: R.Rahmani@lboro.ac.uk

Keywords: flow factors, non-Gaussian surfaces, cross-hatched honing, friction

Abstract

The paper presents a combined numerical and experimental study of generated sliding friction at low sliding speeds and high load intensity, typical of the top compression ring–cylinder liner conjunction at top dead centre in the compression stroke of high performance race engines. Frictional losses in the transition from compression to power stroke represent a significant portion of cyclic cylinder losses. The cylinder liner is cross-hatch honed with non-Gaussian topography, including larger groove features and a fairly smooth plateau roughness. Surface-specific flow factors are derived to closely represent the actual real rough conjunction. The predictions closely agree with the representative reported precision tribometric study of measured friction.

Nomenclature

$\mathscr{A}$	Apparent area of contact
$\tilde{A}$	Mean asperity contact area
a	Acceleration of floating plate arrangement
E'	Composite Young's modulus of elasticity
F_n	Nonlinear function
f	Friction
f_b	Boundary friction
f_v	Viscous friction
h	Local mean surface separation
h_T	Local surface separation
L_x, L_y	Contact length in axial and transverse directions
m	Mass of floating plate arrangement
p	Local hydrodynamic pressure
$\bar{p}$	Mean hydrodynamic pressure
p_{atm}	Atmospheric pressure
$\tilde{P}$	Mean asperity load
$\bar{q}_x$, $\bar{q}_y$	Average flow rate in axial and transverse directions
s	Intermediate variable for nonlinear function
S_a	Arithmetic average of surface variation from mean plane
S_{sk}	Asymmetry measure of surface height probability distributions (Skewness)
t	Time
U_1, U_2	Speed of surfaces 1 and 2 in the axial direction
x, y	Cartesian coordinates in axial and transverse directions

Greek symbols

β	Mean asperity tip radius of curvature
γ	Surface roughness directionality (Peklenik number)
E	Expectation (averaging) operator

η	Lubricant dynamic viscosity
λ	Stribeck film ratio parameter
λ_x	The surface autocorrelation length in the axial direction
ξ	Density of asperity peaks
ρ	Lubricant density
$\sum F$	Net applied force
σ	Composite standard deviation (composite rms of the roughness)
σ_1, σ_2	Standard deviation (rms of the roughness) for surface 1 and 2
ς	Coefficient of the shear strength of the asperities
$\bar{\tau}$	Mean lubricant shear stress
τ_0	Eyring shear stress
Φ_{fs1}, Φ_{fs2}	Shear friction flow factor for surface 1 and 2
Φ_{s1}, Φ_{s2}	Shear flow factor for surface 1 and 2
ϕ_1, ϕ_2	Surface height probability distribution
ϕ^*	Standardised probability distribution (the convolution of ϕ_1 and ϕ_2)
ϕ_c	Density flow factor
ϕ_f	Friction flow factor
ϕ_{fp}	Pressure friction flow factor
ϕ_{fs}	Shear friction flow factor
ϕ_h	Contact flow factor
ϕ_s	Combined shear flow factor
ϕ_x, ϕ_y	Pressure flow factors in the axial and transverse directions

Abbreviations

EN	European standard
VI	Viscosity index

1. Introduction

Reciprocating contacts often experience increased friction because of a mixed regime of lubrication owing to motion reversal and reduced relative motion of surfaces. In the case of piston–cylinder system, this problem occurs at the top and bottom dead centres. In fact, Styles *et al* [1] showed numerically that 30% of the total cyclic friction occurs in transition from the compression to power stroke at the top dead centre. This proportion of frictional losses was also measured directly using a floating liner by Gore *et al* [2] from a fired engine.

Reduction of friction from piston–cylinder system would significantly improve engine fuel efficiency as on average the frictional losses of piston ring pack, comprising two compression rings and an oil control ring can account for up to 5% of the input fuel energy [3]. Therefore, even a small reduction in friction would accrue significant fuel savings and also reduce harmful emissions. The main function of the top compression ring is to seal the combustion chamber, so maintaining a tighter gap with the cylinder liner surface. This yields increased frictional losses as a proportion of the overall ring-pack losses. Therefore, prediction of these losses is essential prior to any palliative action, including surface texturing [4–6] and/or surface coatings [7].

An appropriate modelling approach should take into account surface topography of the contiguous surfaces. Patir and Cheng [8, 9] developed an average flow model, based on Reynolds equation in order to take into account the effect of surface topography on the lubricant flow through a rough conjunction. In such a model various flow factors are utilised to statistically represent the lubricant flow due to different mechanisms of induction.

Three flow factors were used by Patir and Cheng [8, 9] to account for the local pressure: ϕ_x, representing the surface impedance to flow in the direction of entraining motion, ϕ_y, representing the surface impedance to flow in the transverse or side leakage direction and ϕ_s, which accounts for the additional lubricant transport due to the shearing effects, induced by the surface roughness. These flow factors are derived as functions of the Stribeck's oil film parameter ($\lambda = h/\sigma$) [10] and the Peklenik number (γ) [11] which represents the directionality of the surface topography as a function of the autocorrelation functions in the x- and y-directions.

Patir and Cheng [8, 9] provided a generic set of equations for the flow factors for typical surface roughness and directionality. These flow factors have been extensively used in the study of contacts experiencing a mixed regime of lubrication in a wide variety of engineering applications. A number of authors have used this approach to study the contact of compression ring–cylinder liner contact [12–15]. However, Patir and Cheng's generic equations are based on certain assumptions regarding a specific set of surface properties, including a Gaussian distribution of rough surface heights. There have been attempts to address this limitation, such as the work reported by Jocsak [15] who considered generation of flow factors for real surfaces. The study was focused on how surface

parameters such as the skewness of the surface height distribution would affect the predicted friction. The study investigated improvement in prediction for piston ring–cylinder liner conjunction, taking into account the real topography of cylinder liners which are usually cross-hatch honed. The resultant flow factors were calculated using the average Reynolds method and verified experimentally on a reciprocating slider rig, using sections of an actual ring and liner. With curved surfaces used in the test rig it was necessary to avoid the effect of geometric macroscopic form on the generated flow factors. As a result only a small representative area could be considered (of dimensions 0.075 mm in the sliding x-direction and 0.6 mm in the side leakage y-direction).

There have been other attempts to expand the initial work of Patir and Cheng [8, 9]. Of note was the work of Harp and Salant [16] who incorporated the effect of inter-asperity cavitation into the average Reynolds equation through the addition of another flow factor, ϕ_c, to account for the lubricant density fluctuations with inter-asperity cavitation. This approach limits the ease with which the flow factors can be applied as ϕ_c is dependent on the additional variables; lubricant viscosity, sliding velocity, lubricant cavitation vaporization pressure and mean contact pressure as well as λ and γ. The Patir and Cheng method uses flow factors which are only dependent on the topography of surfaces and their separation. Since the surfaces are considered to remain unchanged at all separations the flow factors can be represented as a curve on a graph of the flow factor as a function of surface separation (i.e. λ). Thus, the flow factors with Patir and Cheng approach can be described as a function of λ, making the method far more practical for a wide range of applications. This means that film thickness is all that is needed to predict lubricant load carrying capacity and viscous friction.

Chengwei and Linqing [17] used an analysis of the surface height probability distribution to remove one of the more complex terms from the average Reynolds equation, $\partial \bar{h}_T / \partial h$, and replace it with a flow factor referred to as contact flow factor, ϕ_h. In fact, the parameter ϕ_h expresses the probability that a node in the representative analysis area is not a point of direct contact, thus reducing the burden of computation. They provide a set of curve-fitted functions for estimating ϕ_h. However, the probability distribution fits provided were all symmetrical about its mean which is not usually the case for real engineering surfaces. With the surface data available, it is nonetheless a simple task to calculate ϕ_h for any given surface. The result is specific for a given surface, thus the quality of the data would determine the accuracy of the flow factor.

Knoll *et al* [18] calculated flow factors, taking into account the elastic deformation of the surfaces. This addition alters the area of contact and the topography. This approach would be suitable for elastohydrodynamic contacts. For piston ring–cylinder liner contact elastic deformation of surfaces is shown to be negligible, even for high performance vehicles with significant contact forces [13, 19].

Meng *et al* [20] also considered the elastic deformation of the contacting surfaces as well as the inter-asperity cavitation of Harp and Salant [16]. It was found that for low values of λ these inclusions can be relatively important. However, no experimental validation of the same was provided. Meng *et al* [21] also considered thermal effects and similarly found that this effect can also be important for low values of λ. A drawback in the inclusion of these features is the increased computational costs, which makes the approach less appealing for industrial applications.

Overall, many of the previous studies have been confined to surfaces with assumed Gaussian distribution of surface heights and linear autocorrelation functions where generated surfaces have been used. An important point which has not been considered is that in the internal combustion engine applications the cylinder liner is normally honed (or cross-hatched). Honing is a surface finishing technique that introduces semi-regular features to the surface which dominate the original roughness. An attempt to address the influence of these features is to include a deterministic function such as the one introduced by Spencer *et al* [22]. However, this method normally requires very fine computational meshes which would significantly increase the computational burden. Furthermore, the method cannot be employed together with the average flow model as the surface roughness would no longer have the dominant effect and the conditions for use of average flow model would no longer be satisfied.

This paper considers the application of average flow model for real engineering surfaces such as cylinder liners which also include large scale surface features. There has been a dearth of application of average flow method to non-Gaussian surfaces, where careful consideration is necessary for sampling of surface data, particularly for inclusion of larger surface features. In particular, the case of cross-hatch honed surfaces is considered.

2. Theoretical background

The average flow model employs statistical sampling to represent the rough surfaces and analyses the flow of lubricant flow through their contact. Representative areas of surface topography are sampled under specific conditions so that the effect of surface roughness on different components of flow can be analysed separately. These conditions strive to isolate the flow induced by pressure in the contact directions; x (direction of entraining motion) and y (direction of side leakage), as well as the shear induced flow generated by relative motion of the surfaces. These effects, referred to as flow factors are then included in

the standard Reynolds equation (1), thus forming the average flow equation (2):

$$\frac{\partial}{\partial x}\left(\frac{{h_T}^3}{12\eta}\frac{\partial p}{\partial x}\right)+\frac{\partial}{\partial y}\left(\frac{{h_T}^3}{12\eta}\frac{\partial p}{\partial y}\right)=\frac{U_1+U_2}{2}\frac{\partial h_T}{\partial x}+\frac{\partial h_T}{\partial t}, \tag{1}$$

$$\frac{\partial}{\partial x}\left(\phi_x\frac{h^3}{12\eta}\frac{\partial \bar{p}}{\partial x}\right)+\frac{\partial}{\partial y}\left(\phi_y\frac{h^3}{12\eta}\frac{\partial \bar{p}}{\partial y}\right)=\frac{U_1+U_2}{2}\frac{\partial h}{\partial x}+\frac{U_1-U_2}{2}\sigma\frac{\partial \phi_s}{\partial x}+\frac{\partial h}{\partial t}. \tag{2}$$

The statistical sampling of the surfaces represents the actual topography with an increasing larger sampled area and resolution of measurement, yielding more accurate evaluation of the flow factors.

The average flow model relies on the solution of the standard Reynolds equation for calculating the flow in small representative areas (patches) of the contact. The usual assumptions of Reynolds equation are extended to the average flow method. Further assumptions are applied when solving Reynolds equation for the representative patches of the whole contact area [8]:

- The lubricant is considered to be iso-visocus and incompressible with no cavitation in the representative areas.
- There is no flow at the transverse boundaries of the representative areas or wherever a direct contact occurs.

For the pressure-induced flow factors two rough surfaces are considered to be stationary relative to one another (no relative sliding) with a pressure gradient in one of the Cartesian directions. This results in no shear-induced flow and as the pressure gradient is introduced in a given direction (x or y), the flow in that direction is evaluated. The pressure flow factors are found by analysing the flow rate in comparison to idealised smooth surfaces with the same separations.

For Reynolds equation (1) the flow components in the x- and y-directions are expressed as:

$$\bar{q}_x=\frac{1}{\Delta y}\int_y^{y+\Delta y}\left[-\frac{{h_T}^3}{12\eta}\frac{\partial p}{\partial x}+\left(\frac{U_1+U_2}{2}\right)h_T\right]\mathrm{d}y, \tag{3}$$

$$\bar{q}_y=\frac{1}{\Delta x}\int_x^{x+\Delta x}\left(-\frac{{h_T}^3}{12\eta}\frac{\partial p}{\partial y}\right)\mathrm{d}y. \tag{4}$$

For the average flow model; equation (2), these flow components can be expressed as:

$$\bar{q}_x=-\phi_x\frac{h^3}{12\eta}\frac{\partial \bar{p}}{\partial x}+\left(\frac{U_1+U_2}{2}\right)h+\frac{U_1-U_2}{2}\sigma\phi_s, \tag{5}$$

$$\bar{q}_y=-\phi_y\frac{h^3}{12\eta}\frac{\partial \bar{p}}{\partial y}. \tag{6}$$

Using the above equations, it follows that:

$$\phi_x=\frac{\frac{1}{\Delta y}\int_y^{y+\Delta y}\left(-\frac{{h_T}^3}{12\eta}\frac{\partial p}{\partial x}\right)\mathrm{d}y}{\frac{h^3}{12\eta}\frac{\partial \bar{p}}{\partial x}}, \tag{7}$$

$$\phi_y=\frac{\frac{1}{\Delta x}\int_x^{x+\Delta x}\left(-\frac{{h_T}^3}{12\eta}\frac{\partial p}{\partial y}\right)\mathrm{d}x}{\frac{h^3}{12\eta}\frac{\partial \bar{p}}{\partial y}}. \tag{8}$$

These equations allow the calculation of the pressure flow factor for each discretised region of the surface. To calculate the overall pressure flow factor for a given surface this must simply be averaged over all the discretised regions.

Calculation of the shear flow factor is more complex as the effect of each surface sliding relative to an assumed stationary smooth counter face in the absence of any pressure-induced flow should be evaluated. Therefore, the transportation of lubricant due to its interaction with surface roughness in each direction is obtained. The compound flow factor is a function of Φ_{s1} and Φ_{s2} due to each sliding counter face rough surface, thus:

$$\phi_s=\left(\frac{\sigma_1}{\sigma}\right)^2\Phi_{s1}+\left(\frac{\sigma_2}{\sigma}\right)^2\Phi_{s2}\,. \tag{9}$$

As a result, equations (3) and (5) can be equated and the mean pressure gradient terms can be omitted such that the shear flow factor for each surface would become:

$$\Phi_{s,i}=\frac{\frac{2}{L_xL_y}\int_0^{L_x}\int_0^{L_y}\left(-\frac{{h_T}^3}{12\eta}\frac{\partial p}{\partial x}\right)\mathrm{d}y\mathrm{d}x}{(U_1-U_2)\sigma_i}\quad i=1,\ 2. \tag{10}$$

Simulation of several small representative areas can then be averaged to find the flow factors for the overall contact.

3. Surface-specific flow factors for cross-hatched surfaces

In order to apply the method to real rough surfaces the limitations of the method must be addressed. Patir and Cheng [8, 9] used a computation grid of 25 × 25 points for their analysis with a resolution of approximately three computation points per auto-correlation length (λ_x). Harp and Salant [16] increased the computation matrix to 96 × 96 points and retained the same resolution. A further study by Harp [23] suggested that this level of resolution was adequate, however, both studies use generated Gaussian surfaces with linear autocorrelation functions. A list of attributes used in some previous studies is shown in table 1.

Table 1. Details of some previous studies.

Previous studies	Grid size	Number of grid points per λ_x	Number of statistically identical surface patches
Patir and Cheng [8, 9]	25 × 25	3	10
Teale and Lebeck [24]	26 × 26	4	10
Lunde and Tonder [25]	100 × 100	5 or 10	10
Peeken *et al* [26], Knoll *et al* [18]	80 × 80	14	10
Harp [23]	96 × 96	3	50

Representation of resolution in terms of autocorrelation length has proved to be a suitable measure for generated surfaces with linear autocorrelation functions. However, with real surfaces this approach is often unrepresentative, for example for a cylinder liner surface with cross-hatching. In this case the nominal roughness comprises large scale topographical variations of fabricated grooves and small scale roughness on the formed plateau regions between the grooves. Any determined autocorrelation would be dominated by the large scale variations due to the presence of the grooves, and any resolution based on this would be insufficient for representation of the plateau roughness. In fact, for cross-hatched surfaces both the resolution and sample areas must be considered, because the inclusion of deeper grooves is necessary for an accurate average of their inter-spacing. These grooves induce pressure perturbations in micro-hydrodynamic lubrication, similar to textured surfaces [27]. Therefore, it is necessary to find a suitable set of limits for the resolution and sample area in the current study, which focuses on cross-hatch honed surfaces.

4. Measurement of contacting surfaces

4.1. Topography of contacting surfaces

Test pieces were made for the sliding contact between a flat rough sliding surface (a strip) and a cross-hatched flat surface with similar arithmetic average (S_a), rms (σ) and skewness (S_{sk}) values (see appendix A) to that of a typical cylinder liner (figure 1). The roughness parameters considered are the S_a values quantifying roughness, σ for the calculations of flow factors in the average Reynolds equation, whilst S_{sk} quantifies the degree of non-Gaussian nature of the surface height frequency distributions. The images of the counter face surfaces are shown in figure 1, whilst the topographical parameters are listed in table 2.

The contact profile of the sliding strip comprises a 20 × 20 mm square flat contact face-width with additional 45° chamfers at its leading inlet and trailing outlet zones.

Surface topographies of the counter face surfaces were measured using an Alicona Infinite Focus Microscope with a vertical resolution repeatability of 10 nm and a lateral resolution repeatability of 0.175 μm, using various magnifications: ×5, ×10, ×20, ×50 and ×100. The generated data files contained 1624 × 1232 data points from the surface with approximately 1.76, 0.88, 0.44, 0.18 and 0.09 μm intervals. No form filtering process was employed.

4.2. Measurement sensitivity

In the method outlined by Patir and Cheng [8, 9], the measured surfaces can be analysed with any specified number of data points. An area of the measured surface is then extracted and provided as an input to the numerical analysis. The sampled area and the chosen resolution are considered in such a way that the centre point of the surface remains at the same surface position and thus approaches a more complete representation of the actual contact area locally. Therefore, a larger area becomes statistically more representative of the entire surface area. Furthermore, including more nodes show enhanced details of surface gradient and the generated flow factors would represent the modelled surface more closely. This approach should be set against the increasing computation time with an increasing resolution. Therefore, a sensitivity analysis based upon the measurement resolution and its effect on calculated flow factors is essential.

To examine the resultant flow factors as the measurement resolution is varied, the surface was imaged with the same centre point, but with different measurement resolutions. The same area was then analysed numerically to obtain the flow factors.

Figure 2 shows flow factors with different measurement resolutions. It can be seen that there is considerable variation with magnification of ×5, corresponding to an interval distance of approximately 1.76 μm between the measured areas. Applying an autocorrelation function to the surface, it can be seen that the autocorrelation length is $\lambda_x = 13.88$ μm. This clearly illustrates the issue in applying Gaussian sampling principles to non-Gaussian surfaces. The resolution is not sufficient for consistent results despite the fact that the resolution is well within the three-points per λ_x specified by Patir and Cheng [8, 9] and used by Harp and Salant [16], both of whom used Gaussian generated surfaces. From the results it is clear that the pressure flow factors are more closely grouped and have good consistency with a measurement magnification ×20 or higher, whereas the shear flow factors are closely grouped at magnification of ×50 and beyond. Therefore, a magnification of ×50 is used throughout the current study, which in turn provides a spacing of 0.22 μm between the measured nodes.

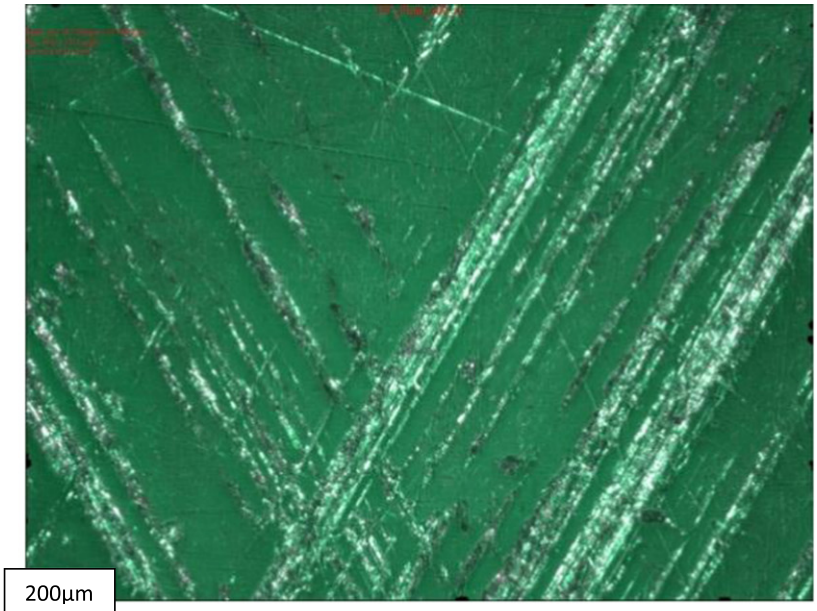

(a) Cross-hatched flat surface

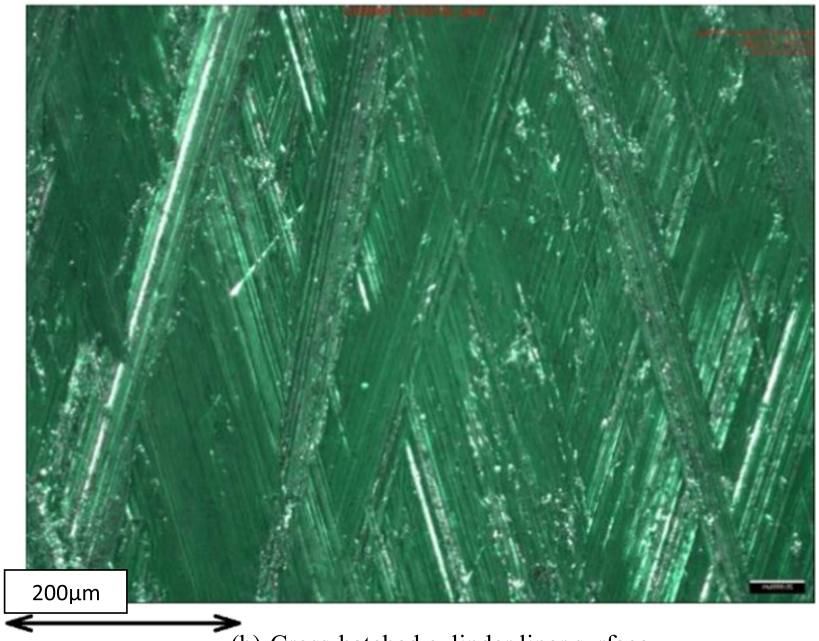

(b) Cross-hatched cylinder liner surface

Figure 1. Interferometric images of cross-hatch honed surfaces (mag: ×20, total area of 712 × 540 μm).

Table 2. Comparison of the test surface topography and that of a cylinder liner surface.

Roughness parameters	Flat cross-hatched surface	Cylinder liner
S_a	341.402 nm	331.710 nm
σ	442.414 nm	421.786 nm
S_{sk}	0.014	0.012

Enlarging the sampled area such that its centre point remains at the centre of the domain also improves the representation of the entire surface. A larger number of sampled areas becomes progressively statistically more representative of the entire surface, thus yielding more accurate evaluated flow factors.

Figure 3 shows the pressure and shear flow factors generated for surfaces with a given resolution, but with different sampled areas. The flow factors are expected to vary with changes of sample areas, except when the surface is topographically repeatable, in which case the average flow factors converge. With consistent machining processes and enhanced quality control, the advanced cylinder liner technology yields good repeatable surface topography as is the case for the representative studied surfaces here (figure 3).

From the graph of pressure and shear flow factors depicted in figure 3, it can be seen that for small areas the results tend to oscillate. Nevertheless, they begin to converge with an increasing number of sampled

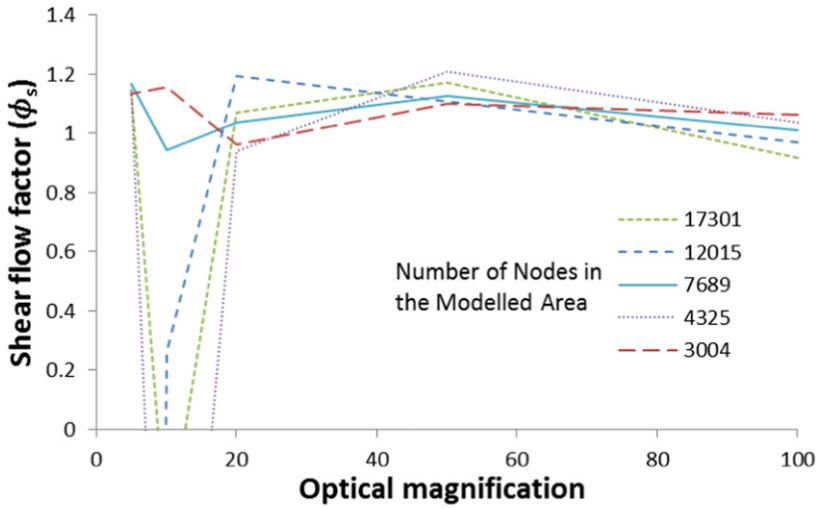

(a) Shear flow factor

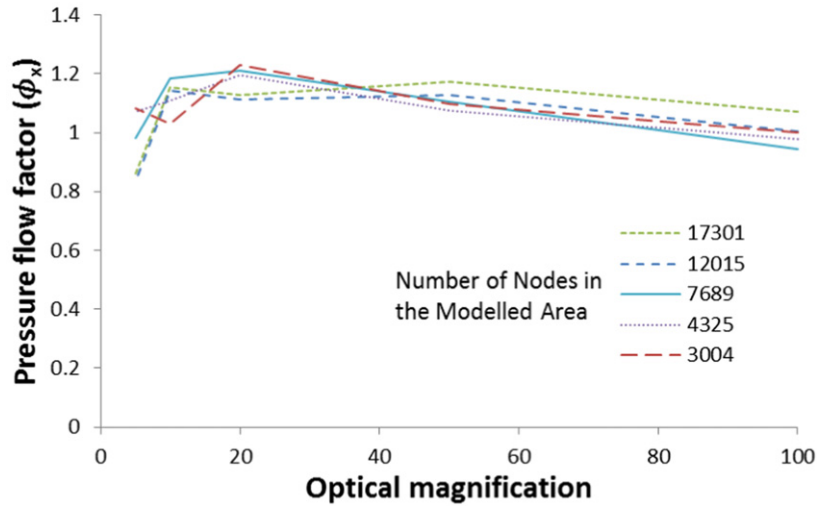

(c) Pressure flow factor

Figure 2. Variation of pressure and shear flow factors with topographical measurement resolution and interferometric optical magnification.

nodes. Since the roughness is on a relatively large scale for the surfaces described here, a large area is required before convergence to a repeatable pattern emerges. A sufficient number of sampled areas should be used so that in practice the sensitivity of evaluated flow factors with sampled area size is diminished. The results show that for the generated pressure flow factors a sampled area with greater than 600 measured points in each lateral direction would suffice, whereas for the shear flow factors 800 measured points per lateral dimension would be required for the typical cross-hatched topography of cylinder liners.

A perturbation study was undertaken to find the variation in flow factors as the number of sampled points were increased. A total of ten sampled areas were used with the aforementioned measurement resolution and area dimensionstudies. The results of the perturbation study are shown in figure 4.

Figure 4 shows that as the sample size increases the spread of the averages of the possible perturbations decreases rapidly and a close grouping is observed before ten samples are used. Therefore, a sample size of ten areas was deemed as sufficient for the current study.

The results presented here correspond to a measurement resolution interval of 0.22 μm between successive points with an optical magnification of $\times$50, sampled areas of 17 301 μm^2 for pressure flow factors (an array 600 $\times$ 600 points), and 30 758 μm^2 for shear flow factors (an array 800 $\times$ 800 points). At least ten representative sampled surface areas are averaged in all cases.

5. Generated pressures and shear flow factors

Figures 5(a) and (b) show pressure flow factors in the axial and transverse directions respectively. These are specific to the cross-hatched surface topography. The

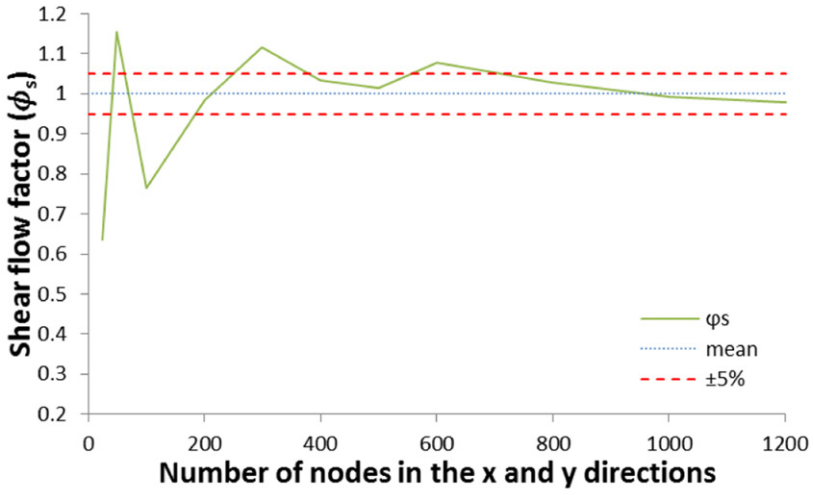

(a) Shear flow factor

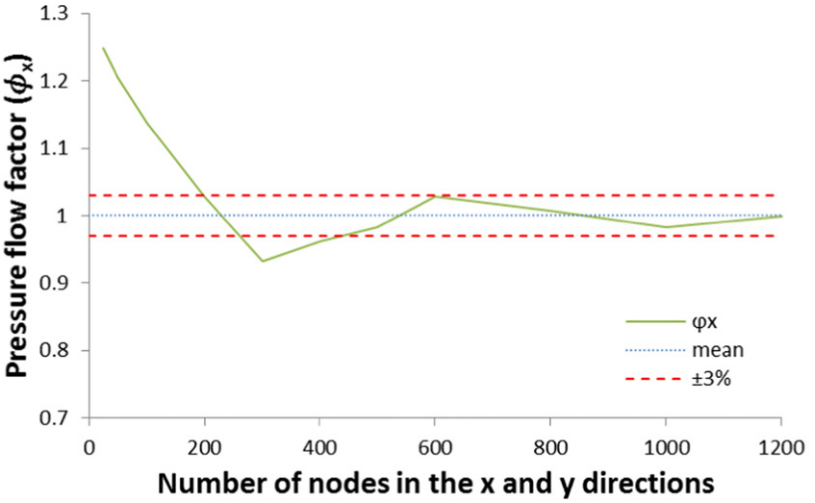

(b) Pressure flow factor

Figure 3. Variation of flow factors with sample surface area.

pressure flow factors are averaged from ten measured sampled areas of the surface, with the limits bounded by a standard deviation at each point as indicated in the figure. The predicted flow factors, using Patir and Cheng [8, 9] approach are also shown in the same figures. The deviation of the surface-specific flow factors from that of Patir and Cheng representation demonstrate the variation found for measured non-Gaussian surfaces. It can be seen that the flow factors found for the measured surfaces closely follow the trend predicted by Patir and Cheng [8, 9] until asperity interactions significantly affect the lubricant flow ($\lambda \approx 2$), where the results commence to diverge significantly. This is due to the difference in the frequency distributions with increasing asperity interactions, because the depth and shape of the flow channels become quite different for lubricant flow. Furthermore, a pair of perfectly plateau honed surfaces (smooth plateaus with valleys) would present little asperity interactions until the plateaus come into contact at low λ values. Alternatively, a perfectly Gaussian surface would begin to experience minor asperity interactions at a higher value of λ, therefore, a more gradual change in performance would be noted with the approach of the counter face surfaces. The measured surfaces used in this study are real rough surfaces and the change in performance from that of a perfectly Gaussian pair is clearly observed.

The curve fit equations for the pressure flow factors are given as 4th order polynomials:

$$\phi_x = 0.0473\lambda^4 - 0.6733\lambda^3 + 3.4993\lambda^2 - 7.9074\lambda + 7.6562, \quad (11)$$

$$\phi_y = 0.0120\lambda^4 - 0.1678\lambda^3 + 0.8195\lambda^2 - 1.5162\lambda + 1.4219. \quad (12)$$

Figures 6(a)–(c) show the shear flow factors in the axial (sliding) direction for the cross-hatched surface and the sliding strip contact face, as well as for the convolution of these. Again, these are based on averaging of ten measured surface regions. The flow factors based on Patir and Cheng's [7, 8] approach have also been included in the figures for the purpose of

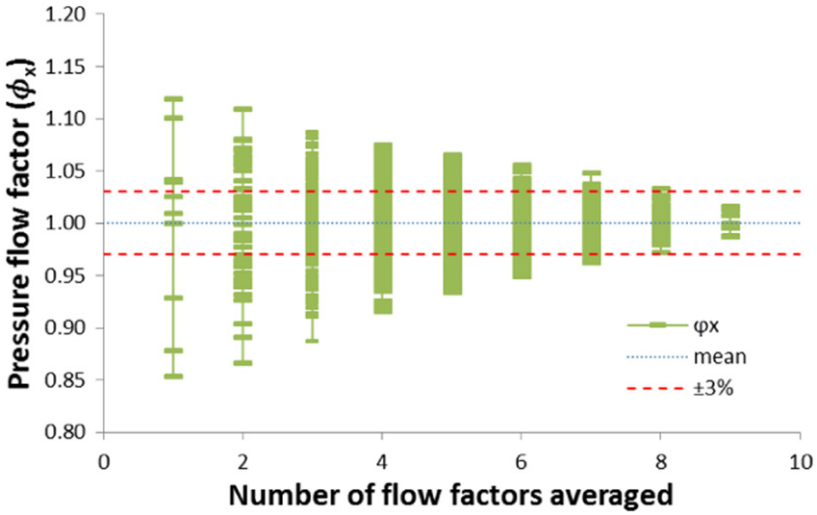

Figure 4. Variation of pressure flow factor with number of sampled areas.

comparison with the surface-specific approach used in the current analysis. It can be seen that the flow factor Φ_{s1} for the measured surfaces closely follows the trend of Patir and Cheng's curve fit flow factors until the film ratio of $\lambda \approx 2$ is reached, where the trends commence to diverge rapidly. In comparison, the flow factor Φ_{s2} for the sliding strip face shows a closer conformity to that of the Patir and Cheng curve fit flow factors because its topography is closer to Gaussian.

The ϕ_s value used in the average Reynolds equation is then determined from a combination of Φ_{s1} and Φ_{s2} through convolution (figure 6(c)).

Again the curve fit equations for the shear flow factors are given as 4th order polynomial curve fits:

$$\Phi_{s1} = -0.0124\lambda^4 + 0.1652\lambda^3 - 0.7505\lambda^2 + 1.1959\lambda + 0.2558, \quad (13)$$

$$\Phi_{s2} = -0.0011\lambda^4 + 0.0092\lambda^3 - 0.0016\lambda^2 - 0.171\lambda + 0.4616, \quad (14)$$

$$\phi_s = -0.0031\lambda^4 + 0.0416\lambda^3 - 0.1947\lambda^2 + 0.3337\lambda + 0.0223. \quad (15)$$

6. Deriving the contact flow factor

Chengwei and Linqing [17] provided curve fit equations for the contact flow factor, ϕ_h, for various surfaces with symmetrical surface height distributions. The contact flow factor can be considered as the probability that a discrete point is not in contact for a given film ratio, λ. For Gaussian surfaces $\phi_h \approx 1$ when $\lambda > 3$ and $\phi_h \to 0$ as $\lambda \to 0$. This holds true for many surfaces, but it varies for mixed and/or elastohydrodynamic regimes of lubrication. Therefore, an appropriate representation is essential.

The contact factor is defined as:

$$\phi_h = \frac{\partial \bar{h}_T}{\partial h} = \int_{-\lambda}^{\infty} \phi^*(s) \cdot ds, \quad (16)$$

where, ϕ^* is the standardised surface height distribution. As ϕ^* is for an equivalent surface, then, ϕ^* is the convolution of ϕ_1 and ϕ_2 for the mating surfaces.

Figure 7 shows that the contact factor for the measured surfaces provides similar results to a Gaussian surface with some slight variations in the mixed regime of lubrication.The measured data curve predicts the onset of contact at approximately $\lambda \approx 4$, whereas the formula given for the Gaussian curve by Patir and Cheng [8, 9] precludes this until $\lambda < 3$. Thereafter, the measured surface results remain slightly higher than a Gaussian surface. This means that although first contact is predicted to occur sooner than for a Gaussian surface, $\lambda \approx 4$, the area of the contact remains smaller in the region $\lambda < 3$.

The curve fit equations for the contact flow factor are:

$$\phi_h = 0.0001\lambda^6 - 0.0008\lambda^5 - 0.0026\lambda^4 + 0.0656\lambda^3 - 0.3379\lambda^2 + 0.7441\lambda + 0.3800. \quad (17)$$

7. Deriving the shear stress factors

In addition to the commonly used pressure and shear flow factors, Patir and Cheng [8, 9] also determined a series of empirical flow factors which allow the calculation of viscous friction. These are given as ϕ_f, ϕ_{fp} and ϕ_{fs}. ϕ_f accounts for the average sliding velocity component of the shear stress, ϕ_{fp} is a correction factor for the mean pressure flow component of the shear stress and ϕ_{fs} is the correction factor for the combined

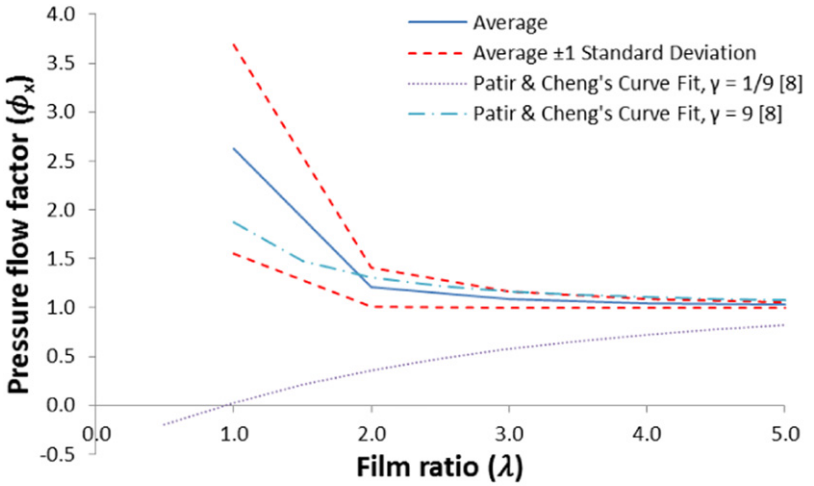

(a) In the axial direction

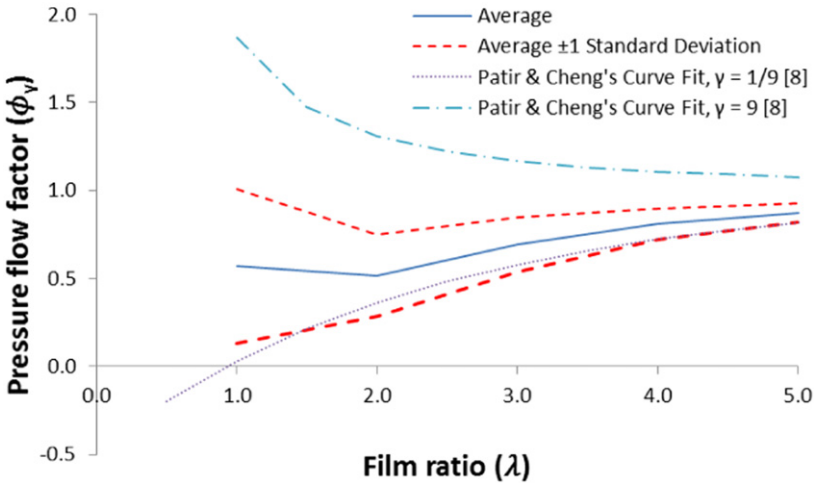

(b) In the transverse direction

Figure 5. Generated pressure flow factors.

effect of sliding roughness. Each of these friction factors has a similarity with other flow factors already calculated: ϕ_f, ϕ_{fp} and ϕ_{fs} can be considered analogous to ϕ_h, ϕ_x and ϕ_s, respectively. The parameter ϕ_f is calculated from the frequency distribution of the surface roughness, ϕ_{fp} is calculated from a simulation of the pressure within a representative area when the two surfaces are considered as stationary relative to each other and ϕ_{fs} is calculated from simulation of each representative area, sliding against a smooth counterpart, surface without an overall pressure gradient. These flow factors have also been calculated from equations below and the results are shown in figures 8, 9 and 10. Since ϕ_f, like ϕ_h, is considerably quicker to calculate, more data points have been taken for the same range of λ values that were considered for the other flow factors.

$$\phi_f = hE\left(\frac{1}{h_T}\right), \tag{19}$$

$$\phi_{fp} = \frac{\dfrac{1}{\Delta y}\displaystyle\int_y^{y+\Delta y}\left(-\frac{h_T}{12\eta}\frac{\partial p}{\partial x}\right)\mathrm{d}y}{\dfrac{h}{12\eta}\dfrac{\partial \bar{p}}{\partial x}}, \tag{20}$$

$$\Phi_{fsi} = \frac{\dfrac{h}{L_x L_y}\displaystyle\int_0^{L_x}\int_0^{L_y}\left(-h_T\frac{\partial p}{\partial x}\right)\mathrm{d}y\mathrm{d}x}{2\eta(U_1 - U_2)}, \tag{21}$$

$$\phi_{fs} = \left(\frac{\sigma_1}{\sigma}\right)^2\Phi_{fs1} - \left(\frac{\sigma_2}{\sigma}\right)^2\Phi_{fs2}. \tag{22}$$

These figures show a similarity to the curves between the various calculated flow factors and provided by Patir and Cheng [8, 9], using their curve fit expressions. In figure 8, the shear stress factor, ϕ_f and its counterpart from Patir and Cheng [8, 9] for a Gaussian surface follow approximately the same trend until $\lambda \approx 2$, where the characteristics commence to diverge. This is likely to be due to the highly skewed nature of the surfaces at closer separations with the truncation of the initial peak pair contacts.

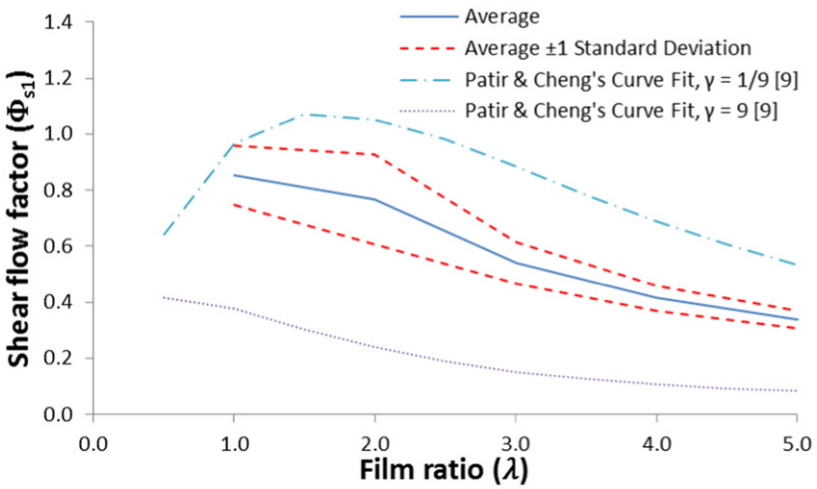

(a) For the cross-hatched honed surface

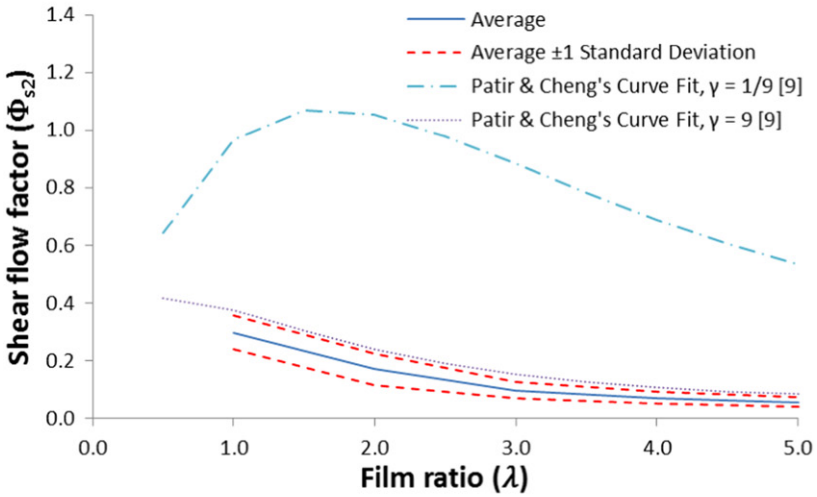

(b) For the sliding strip face

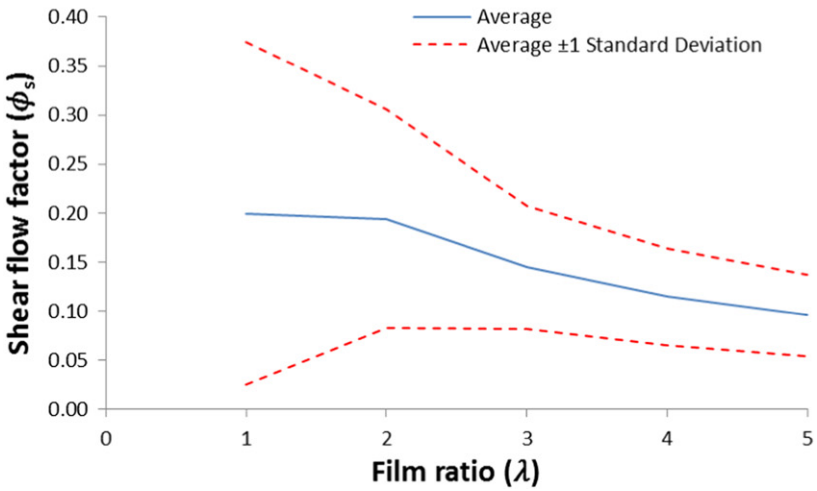

(c) For convoluted counter face surfaces

Figure 6. Generated shear flow factors.

The two partial shear stress factors; Φ_{fs1} and Φ_{fs2}, shown in figures 10(a) and (b), mainly fall within the range of Gaussian surfaces with roughness orientations that were considered by Patir and Cheng [8, 9]. On the other hand, Φ_{fs1} shows some variation from this range at both higher and lower values of λ. It is considered

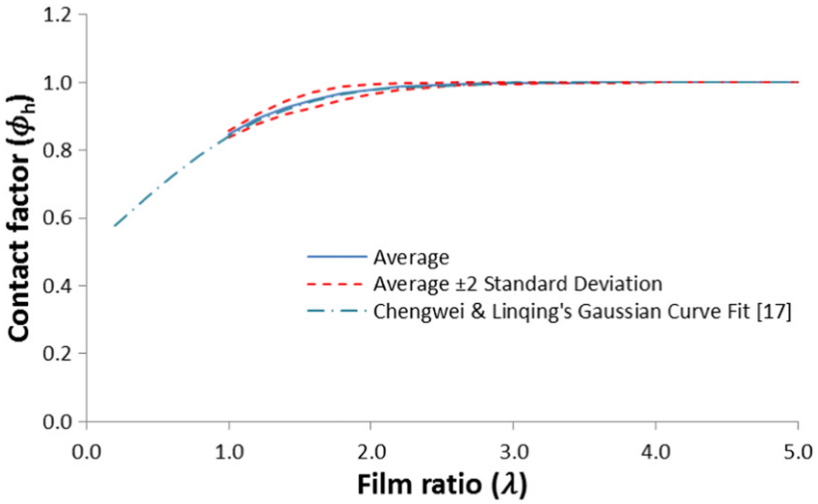

Figure 7. Derived contact factors.

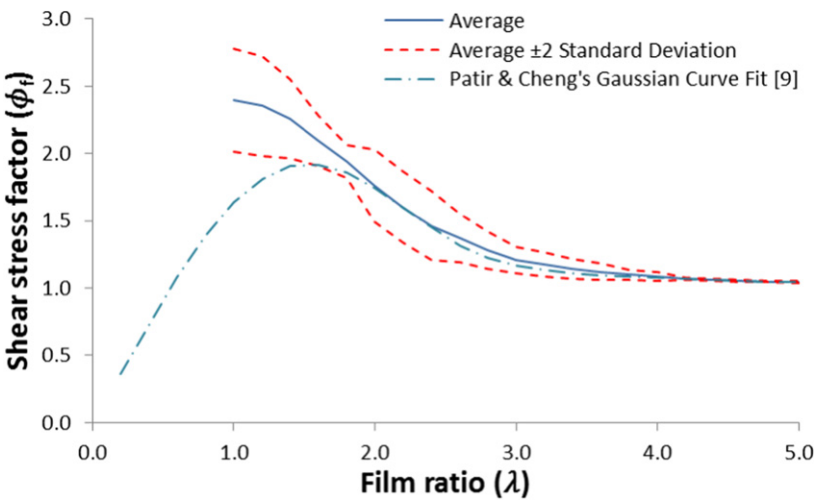

Figure 8. The variation of shear stress factor ϕ_f.

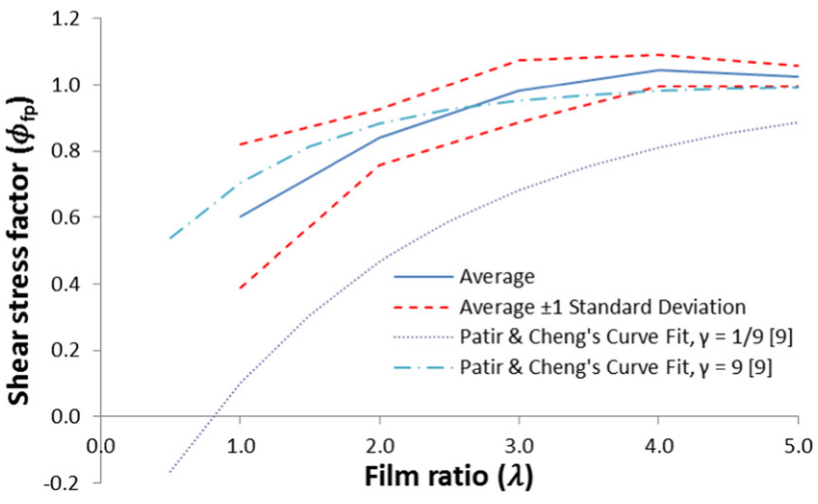

Figure 9. The variation of shear stress factor ϕ_{fp}.

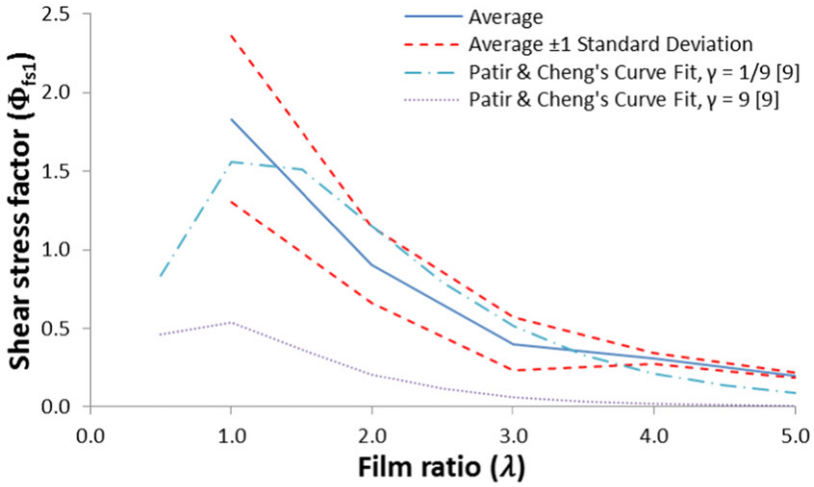

(a) Sear stress factor for the cross-hatched surface, Φ_{fs1}

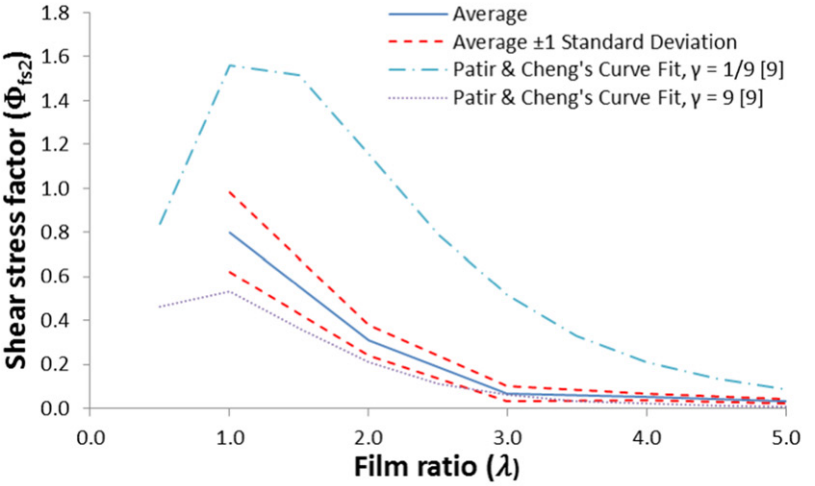

(b) Shear stress factor for the sliding strip face, Φ_{fs2}

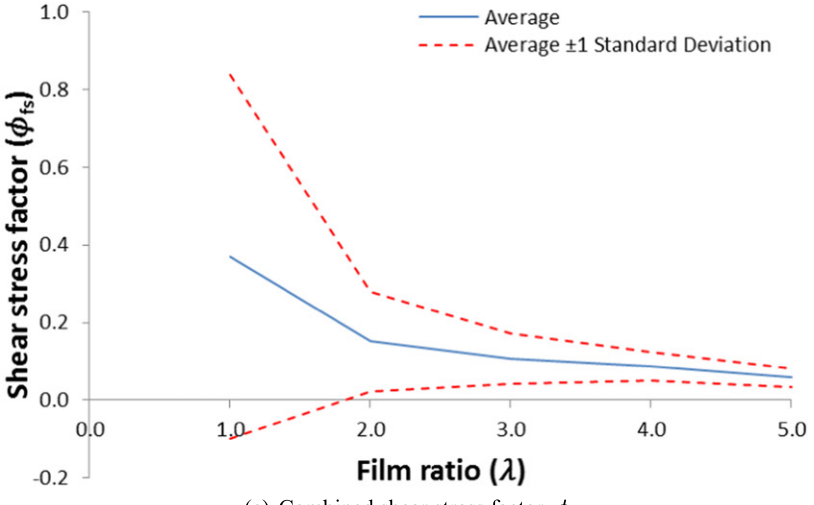

(c) Combined shear stress factor, ϕ_{fs}

Figure 10. Shear stress factors.

that the skewness of the cross-hatched flat surface results in a high lubricant transport rate which decreases as the separation approaches the plateau height before increasing again as the grooves left by the cross-hatching convey a larger volume than the pockets left in a Gaussian truncated surface.

The curves fitted to the shear stress factors are:

$$\phi_f = -0.0029\lambda^6 + 0.0691\lambda^5 - 0.6617\lambda^4 + 3.1824\lambda^3 - 7.8648\lambda^2 + 8.6499\lambda - 0.9806, \quad (23)$$

$$\phi_{fp} = -0.0010\lambda^4 + 0.0140\lambda^3 - 0.1076\lambda^2 + 0.4776\lambda + 0.2213, \quad (24)$$

$$\Phi_{fs1} = -0.0174\lambda^4 + 0.1718\lambda^3 - 0.3847\lambda^2 - 0.7133\lambda + 2.7739, \quad (25)$$

$$\Phi_{fs2} = -0.0087\lambda^4 + 0.0828\lambda^3 - 0.1553\lambda^2 - 0.4750\lambda + 1.3561, \quad (26)$$

$$\phi_{fs} = 0.0050\lambda^4 - 0.0749\lambda^3 + 0.4121\lambda^2 - 1.0054\lambda + 1.0331. \quad (27)$$

8. Determination of contact friction

Contact friction comprises viscous shear of lubricant in flow through the rough counter face surfaces, as well as friction generated by the direct interaction of asperities on the counter face surfaces. Having established the shear flow factors, the viscous component of friction becomes:

$$f_v = \bar{\tau}(\mathscr{A} - \tilde{A}), \quad (28)$$

where:

$$\bar{\tau} = \frac{\eta(U_2 - U_1)}{h}(\phi_f \pm \phi_{fs}) \pm \phi_{fp}\frac{h}{2}\frac{\partial \bar{p}}{\partial x}. \quad (29)$$

To determine the contribution due to asperity friction, the Greenwood and Tripp's model is used in the current analysis [28]. It is noteworthy that this model is based on the assumption of a Gaussian distribution of asperity heights on an equivalent surface against a perfectly smooth semi-infinite elastic half-space. Therefore, in adopting the same, it is assumed that asperity interactions primarily occur on the plateau formed by the cross-hatch honing of the plate sample. This is a reasonable assumption under mixed regime of lubrication as indicated in the results of figure 10; with $\lambda \geqslant 2$ for the case of surfaces used here. As already noted above, after the limiting value of $\lambda \approx 2$ (figure 10(c)) the flow pattern alters significantly from that for a Gaussian surface, because of the additional channels provided by the cross-hatched grooves. This finding is in line with the fired engine tests reported by Gore *et al* [29] who show that wear hardly affects the groove depths as represented by the statistical parameter, R_{vk} (average depth of grooves). Hence, boundary friction is mainly due to the asperity interactions on the plateau surface.

According to Greenwood and Tripp [28], the probabilistic load at a given surface separation can be determined from a combination of an assumed surface topography and elastic deformation of interacting asperity pairs in accord with the classical Hertzian theory, thus:

$$\tilde{P}(h) = \frac{16\sqrt{2}}{15}\pi(\xi\beta\sigma)^2 E' \sqrt{\left(\frac{\sigma}{\beta}\right)}\mathscr{A}F_{\frac{5}{2}}(\lambda), \quad (30)$$

where:

$$F_n(\lambda) = \int_\lambda^\infty (s - \lambda)^n \phi^*(s) \cdot ds. \quad (31)$$

Similarly, the area of asperity contact becomes:

$$\tilde{A}(h) = \pi^2(\xi\beta\sigma)^2\mathscr{A}F_2(\lambda). \quad (32)$$

The $F_n(\lambda)$ functions in equations (30) and (32) can be determined using equation (31). This equation uses the term $\phi^*(s)$ which represents the convolution of the peak height distributions of the contacting rough surfaces.

Boundary friction is due to the interaction of asperities on the counter faces, as well as any pockets of lubricant entrapped between them, which are assumed to be subject to the limiting Eyring [30] shear stress, τ_0, and is given by [31]:

$$f_b = \tau_0\tilde{A} + \varsigma\tilde{P}, \quad (33)$$

where, $\tilde{P}$ is given by equation (30) and $\tilde{A}$ is given by equation (32). The first term on the right-hand side of equation (33) represents the non-Newtonian shear of thin pockets of lubricant entrapped between the contacting asperity pairs. The second term corresponds to the direct interaction of asperities. ς is the coefficient of shear strength of asperities (for the lubricant used: $\tau_0 = 2$ MPa and for steel surfaces: $\varsigma = 0.17$ [31]).

There are three surface-specific parameters; ξ, β and σ. ξ and β can be simply calculated from the surface topography data by identifying asperities as points which protrude above the surrounding topography. For the measured surfaces in this study the Greenwood and Tripp input parameters are:

$$\xi = 0.0206\ \mu m^{-2}, \quad (34)$$

$$\beta = 6.604\ \mu m, \quad (35)$$

$$\sigma = 0.741\ \mu m. \quad (36)$$

Assuming identical surfaces in contact, then $\xi\beta\sigma = \xi\beta\sigma_1\sqrt{2}$ and therefore the range of $\xi\beta\sigma$ values becomes approximately 0.042–0.071 [28]. As a result Greenwood and Tripp [28] use a value of 0.05. For the surfaces considered in this study $\xi\beta\sigma$ is found to be 0.101. This is close to the range expected by Greenwood and Williamson [32], but there is a low combined rms because of the skewed surface height distribution and a large asperity radii on the plateau.

Finally, the total friction becomes:

$$f = f_v + f_b. \quad (37)$$

9. Numerical solution

The boundary conditions used for the solution of the average flow equation (2) in the case of contact configuration described in section 10 comprises atmospheric pressure at the inlet and outlet in the axial and radial directions. Swift–Stieber boundary conditions are applied at the film rupture point, where the

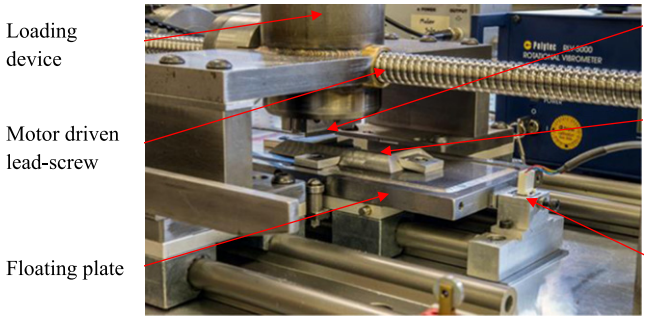

Figure 11. The sliding tribometer.

cavitation pressure is the atmospheric pressure of the lubricant at the environmental temperature of 20 °C.

A second order finite difference method is used to solve the average flow equation (2) by utilising a point-successive over-relaxation scheme. An initial estimation of the minimum film thickness is made and pressure convergence is sought. Convergence is deemed as obtained when the error between successive iterations of generated pressure falls below 1×10^{-6}. The lubricant contribution to load carrying capacity is then found as:

$$W_{\mathrm{hy}} = \int\int p \cdot \mathrm{d}x \cdot \mathrm{d}y. \tag{38}$$

The asperity load carrying capacity is then calculated using the Greenwood and Tripp model [28] using equation (30). The total load carrying capacity of the conjunction at the assumed separation can then be calculated as:

$$W = W_{\mathrm{hy}} + \tilde{P}(h). \tag{39}$$

The load carried is then compared with the applied contact load and a new estimation of the film thickness is made. This iterative procedure is repeated until the error between the calculated contact load and that applied falls below 1×10^{-6}.

10. Numerical results and experimental validation using a precision sliding tribometer

The methodology outlined above is validated against experimental measurement of friction using a sliding tribometer, operating under mixed and boundary regimes of lubrication. Figure 11 shows the precision sliding tribometer used to directly measure the conjunctional friction.

The cross-hatched specimen (described in section 4) is mounted onto a flat plate which is allowed to float freely on low friction bearings. The sliding strip is loaded onto the mounted specimen and motorised to slide via a backlash free low friction lead-screw arrangement. A thin layer of lubricant is supplied to the surface of the cross-hatched specimen. The generated contact friction drags the floating plate, whose inertial dynamics is measured by a pair of piezo-resistive load cells as shown in figure 11, where:

$$\sum F = -f + ma. \tag{40}$$

This arrangement is analogous to the floating liner principle used for measurement of in-cylinder friction as described by Furuhama and Sasaki [33] and Gore *et al* [2], except that the extraneous effects caused by heat generated by combustion in an engine are avoided under these simulated conditions, with required precision measurements intended for validation of the calculated flow factors. Morris *et al* [27] provide further detailed information about the sliding tribometer, showing that the applied load intensity (load per unit length of the sliding strip) and its relative speed are representative of engine conditions at low speed transition from the compression to the power stroke through the top dead centre. The prevailing regime of lubrication under these conditions is mixed-hydrodynamics, which accounts for a significant proportion of engine's frictional power loss as shown by Styles *et al* [1].

A series of tests of short run-time were carried out to measure conjunctional friction with insignificant changes to counter face surface topographies. To ensure repeatable testing conditions a grade 3 base oil stock of highly paraffinic ultra-low sulphur (viscosity index; VI $>$ 125) was used in order to guard against any adsorption or adherence of boundary active additive species which are usually present in formulated lubricants. A laser Doppler vibrometer is used to record the actual speed of the sliding head. Further data for the base oil is listed in table 3. All tests are carried out at atmospheric pressure and at the laboratory temperature of 20 °C.

The test strip and cross-hatched flat specimen are made of EN 14 steel. The data for contacting surfaces and the operational conditions are listed in table 4.

The test pieces produced for this study have been measured and analysed with the Patir and Cheng average flow model [8, 9] and Greenwood and Tripp asperity model [28]. The result of these investigations can be

Table 3. Base oil data.

Parameter	Value	Unit
Eyring shear stress (τ_o)	2	MPa
Lubricant density (ρ)	839.3 @ 20 °C	Kg m^{-3}
Lubricant dynamic viscosity (η)	0.1583 @ 20 °C	Pa s

Table 4. Sliding strip, the cross-hatched surface data and the sliding test conditions.

Parameter	Value	Unit
Flat cross-hatched surface rms roughness (σ_1)	0.442	μm
Strip contact face rms roughness (σ_2)	0.587	μm
Strip face width	20	mm
Strip length	20	mm
Load	16.234	N
Stroke length	50	mm
Mean sliding speed	24	mm s^{-1}

compared with the experimental measurements to validate the model.

Friction measurements are averaged over a 10 mm region of constant sliding speed at the end of the sliding head strokes. 850 friction measurements were taken for each test. Friction was measured for ten separate strokes of the rig and good agreement (repeatability) was noted between these tests. The results of the slider rig tests and the predicted friction from simulations using Reynolds equation, Patir and Cheng's average flow model (with orientation set to 1, 1/6 and 1/9) and the average flow model using the flow factors generated in this study are shown figure 12.

Figure 12 shows that the better agreement is found between the predicted friction using the surface-specific flow factor model for non-Gaussian cross-hatched surfaces, developed in the current study and the experimental measurements than for other models. Clearly, the derived surface-specific flow factors better represent the non-Gaussian surface topography of the cross-hatched specimen, particularly the channels represented by the fabricated grooves as the mixed or boundary regimes of lubrication become prevalent as in the case of the reported experiment (representing low speed sliding). Clearly, use of Reynolds equation, without inclusion of distributed surface roughness leads to an under-estimation of friction. The results for assumed Gaussian distribution of peak heights and lack of taking groove flow channels into account yields over-estimation of friction with Patir and Cheng method [8, 9].

11. Conclusions

Friction is a major source of energy dissipation in many machines and mechanisms. Therefore, except in very few circumstances, such as in traction drives and locomotion, minimisation of frictional losses is often sought. Direct asperity interactions as well as flow of lubricant through rough surfaces give rise to friction. Therefore, surface topography plays a significant role and in prediction of friction it should be taken into account in an appropriate manner, representative of real rather than idealised rough surfaces. The current study shows the non-Gaussian nature of cylinder liner surfaces in internal combustion engines and demonstrates the need to develop appropriate flow factors, necessary for accurate prediction of friction. In particular surface-specific flow factors show much better prediction of friction for simulated contact of top compression ring against a cross-hatch honed cylinder for low speed mixed or boundary regimes of lubrication, representative of top dead centre reversal. This conjunction can account for up to 5% of expended fuel energy through frictional losses. Therefore, the accurate prediction of friction has a significant practical importance for the honing process, leading to palliation of some of these losses.

Acknowledgments

The authors wish to express their gratitude to the Engineering and Physical Sciences Research Council for the financial support of Encyclopaedic Program Grant: www.encyclopaedic.org, under which this research was carried out. The authors also would like to acknowledge the technical support of industrial partners of Encyclopaedic, particularly Capricorn Automotive Ltd (manufacturers of advanced cylinder liner technology) and Castrol the suppliers of lubricant.

Appendix A

The definitions for the statistical surface roughness parameters are:

S_a is the arithmetic mean of the variation for measured heights, z_i from the mean centre-line of the surface:

$$S_a = \frac{1}{n}\sum_{i=1}^{n} z_i. \quad \text{(A1)}$$

σ is the quadratic mean of the variation of measured heights from the mean centre-line of the surface. It is also the standard deviation if the mean centre-line is set to zero

$$\sigma = \sqrt{\frac{1}{n}\sum_{i=1}^{n} {z_i}^2}. \quad \text{(A2)}$$

S_{sk} is the skewness which is a measure of the asymmetry of the probability distribution. A value of zero indicates perfect symmetry; a Gaussian distribution. Positive skewness indicates an extended 'tail' for the distribution exceeding its mean value. Negative

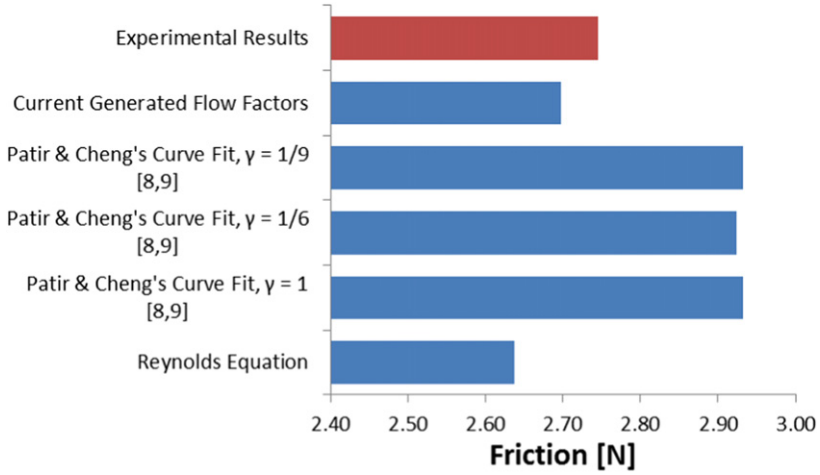

Figure 12. Comparison of friction results with experimental tests for various models.

skewness indicates that the tail of the distribution is more stretched below its mean

$$S_{sk} = \frac{1}{n\sigma^3}\sum_{i=1}^{n} z_i{}^3. \quad \text{(A3)}$$

S_{ku} is the kurtosis which is a measure of the peakedness of the probability distribution and can be considered as a ratio of height-to-width of the distribution. A value of 3 indicates that the data is distributed about the mean in a manner similar to that of a Gaussian distribution. A value exceeding 3 indicates that the majority of the data is clumped around the mean but the outlying points significant great variation.

$$S_{ku} = \frac{1}{n\sigma^4}\sum_{i=1}^{n} z_i{}^4. \quad \text{(A4)}$$

Cross-hatch honed surfaces typically have negative skewness values and a kurtosis value greater than 3.

References

[1] Styles G, Rahmani R, Rahnejat H and Fitzsimons B 2014 In-cycle and life-time friction transience in piston ring–liner conjunction under mixed regime of lubrication *Int. J. Engine Res.* **15** 862–76

[2] Gore M, Theaker M, Howell-Smith S, Rahnejat H and King P D 2014 Direct measurement of piston friction of internal-combustion engines using the floating-liner principle *Proc. IMechE* D **228** 344–54

[3] Holmberg K, Andersson P and Erdemir A 2012 Global energy consumption due to friction in passenger cars *Tribol. Int.* **47** 221–34

[4] Etsion I 2010 *Surface Texturing for in-Cylinder Friction Reduction* (New Delhi: Woodhead Publishing Ltd) pp 458–69

[5] Rahnejat H, Balakrishnan S, King P D and Howell-Smith S 2006 In-cylinder friction reduction using a surface finish optimization technique *Proc. ImechE* D **220** 1309–18

[6] Ryk G, Kligerman Y, Etsion I and Shinkarenko A 2005 Experimental investigation of partial laser surface texturing for piston–ring friction reduction *Tribol. Trans.* **48** 583–8

[7] Howell-Smith S, Rahnejat H, King P D and Dowson D 2014 Reducing in-cylinder parasitic losses through surface modification and coating *Proc. IMechE* D **228** 391–402

[8] Patir N and Cheng H S 1978 An average flow model for determining effects of three-dimensional roughness on partial hydrodynamic lubrication *Trans. ASME, J. Lubr. Technol.* **100** 12–7

[9] Patir N and Cheng H S 1979 Application of average flow model to lubrication between rough sliding surfaces *Trans. ASME, J. Lubr. Technol.* **101** 220–30

[10] Stribeck R 1907 'Die Wesentliechen ichen Eigenschaften Gleit und Rollen Lager' or 'Ball Bearings for various loads' *Trans. ASME* **29** 420–63

[11] Peklenik J 1967 New developments in surface characterisation and measurement by means of random process analysis *Proc. IMechE* **182** 108–26

[12] Tian T, Wong V W and Heywood J B 1996 'A piston ring-pack film thickness and friction model for multigrade oils and rough surfaces *SAE Technical Paper No.* 962032

[13] Akalin O and Newaz G M 2001 Piston ring–cylinder bore friction modeling in mixed lubrication regime: I. Analytical results *Trans ASME, J. Tribol.* **123** 211–8

[14] Hu Y, Cheng H S, Arai T, Kobayashi Y and Aoyama S 1994 Numerical simulation of piston ring in mixed lubrication—a nonaxisymmetrical analysis *Trans ASME, J. Tribol.* **116** 470–8

[15] Jocsak J 2005 The effects of surface finish on piston ring-pack performance in advanced reciprocating engine systems *PhD Thesis* MIT, USA

[16] Harp S and Salant R F 2001 An average flow model of rough surface lubrication with inter-asperity cavitation *Trans ASME, J. Tribol.* **123** 134–43

[17] Chengwei W and Zheng L 1989 An average Reynolds equation of partial lubrication with a contact factor *Trans. ASME , J. Tribol.* **111** 188–91

[18] Knoll G, Rienacker A, Lagermann V and Lechtape-Gruter R 1998 Effects of contact deformation on flow factors *Trans ASME, J. Tribol.* **120** 140–2

[19] Mishra P C, Balakrishnan S and Rahnejat H 2008 Tribology of compression ring-to-cylinder contact at reversal *Proc. IMechE J.* **222** 815–26

[20] Meng F M, Wang W Z, Hu Y Z and Wang H 2007 Numerical analysis of combined influences of inter-asperity cavitation and elastic deformation on flow factors *Proc. IMechE* C **221** 815–27

[21] Meng F M, Cen S Q, Hu Y Z and Wang H 2009 On elastic deformation, inter-asperity cavitation and thermal effects on flow factors *Tribol. Int.* **42** 260–74

[22] Spencer A, Almqvist A and Larsson R 2011 A semi-deterministic texture-roughness model of the piston ring–cylinder liner contact *Proc. IMechE J.* **225** 325–33

[23] Harp S 2000 A computational method for evaluating cavitating flow *PhD Thesis* Georgia Tech., USA

[24] Teale J L and Lebeck A O 1980 An evaluation of the average flow model for surface roughness effects in lubrication *Trans ASME, J. Lubr. Technol.* **102** 360–6
[25] Lunde L and Tonder K 1997 Pressure and shear flow in a rough hydrodynamic bearing, flow factor calculation *Trans. ASME, J. Tribol.* **119** 549–55
[26] Peeken H J, Knoll G, Rienäcker A, Lang J and Schönen R 1997 On the numerical determination of flow factors *Trans. ASME, J. Tribol.* **119** 259–64
[27] Morris N, Leighton M, De la Cruz M, Rahmani R, Rahnejat H and Howell-Smith S 2015 Combined numerical and experimental investigation of the micro-hydrodynamics of chevron-based textured patterns influencing conjunctional friction of sliding contacts *Proc. IMechE J.* **229** 316–33
[28] Greenwood J and Tripp J 1971 The contact of two nominally flat rough surfaces *Proc. Inst. Mech. Eng.* 625 625–33
[29] Gore M, Perera M, Styles G, King P D and Rahnejat H 2011 Wear characteristics of advanced honed and cross-hatched coated cylinder liners *Proc. 66th Annual Meeting and Exhibition of the STLE* p 73
[30] Eyring H 1936 Viscosity, plasticity, and diffusion as examples of absolute reaction rates *J. Chem. Phys.* **4** 283–91
[31] Teodorescu M, Kushwaha M, Rahnejat H and Rothberg S J 2007 Multi-physics analysis of valve train systems: from system level to microscale interactions *Proc. IMechE* K **221** 349–61
[32] Greenwood J and Williamson J 1966 Contact of nominally flat surfaces *Proc. R. Soc. Lond.* **295** 300–19
[33] Furuhama S and Sasaki S 1983 New device for the measurement of piston frictional forces in small engines *SAE Technical Paper* No. 831284